9 Magnetic Measurements in Plant Electrophysiology

Zvonko Trontelj,[1] Gerhard Thiel,[2] Vojko Jazbinsek[1]

9.1 Introduction

Plants show a huge range of dynamic electrical phenomena, including triggered (Umrath 1929) and autonomous action potentials (AP) (Gradmann et al. 1993), or stimulus-evoked slow transient depolarizations (Roblin and Bonnemain 1985). This electrical activity can comprise singular events (Umrath 1929), trains of periodic activity (Williams and Pickard 1972) or even long lasting periodic oscillations of the membrane voltage (Gradmann et al. 1993). Electrical activity can occur in single cells (Gradmann 1976; Bauer et al. 1997) as well as in complex plant tissues (Bentrup 1979). Many of these electrical phenomena resemble electrical activity in animal cells, and by pure analogy it has been proposed that plant cells may function like nerves, and that plants may even have the equivalent of a nervous system (Baluska et al. 2005). Irrational views like these are only possible on the background of a serious ignorance of the physics and molecular basis of electrical activity in plants. Currently we neither really understand the elementary mechanisms underlying electrical activity in plants on the same level as for example the action potential in animal cells, nor do we have clear-cut ideas on their physiological roles. In most cases also, the cellular connections and pathways that propagate electrical activity are not yet certain. Consequently, the mechanistic basis for propagation of electrical activity is also not resolved; it is still a matter of debate whether the signal is really propagated electrically like in nerves or the result of a traveling chemical wave.

The application of new experimental methods such as patch clamp technology (Okihara et al. 1991; Homann and Thiel 1994) has in the past 2 decades brought some deeper insight into the molecular basis of membrane excitation in plants. Combination of classical electrophysiology with fluorescent markers (Rhodes et al. 1996) or molecular sensors (Pena-Cortes et al. 1995) is now also paving the way to address fundamental questions on long distance propagation. A new promising method to address many of these open questions is provided by the magnetic measurements of electrical

[1] Physics Department, IMFM, University of Ljubljana, 1000-Ljubljana, Slovenia (e-mail: zvonko.trontelj@fmf.uni-lj.si)

[2] Institute for Botany, Plant Biophysics, Darmstadt University of Technology, D-64287, Darmstadt, Germany

Plant Electrophysiology – Theory & Methods (ed. by Volkov)

activity in plants. This non-invasive method presents a tool for both high-resolution recordings on the cellular level and time resolved imaging of electrical activity over a whole plant. The present review guides through the theoretical background of the method and shows its application in a few case studies.

9.2 On SQUID sensors

A suitable method to obtain electric current is by measuring the magnetic field and calculating the current by applying Ampère's law or Biot-Savart's law. This method has in addition the advantage of being non-disturbing—what is more than non-invasive—it does not even touch the current source. The frequency of measured current is also an important parameter. High frequency currents can be easily detected even if they are very weak. On the other side, weak quasi-dc or even dc currents are not easily detected magnetically.

The promising magnetic detector of weak quasi-dc currents became operational with the development of superconducting quantum interference devices, known by the acronym SQUID. These most sensitive sensors for low frequency magnetic fields are available since early the 1970s (Zimmerman et al. 1970). Today, they have improved to the extent that we can also measure the very weak human brain signals and practically all other electrophysiological signals in living organisms.

What is the SQUID (See for instance Tinkham 1996) and how does it work? The quick answer is: SQUID is a very sensitive magnetic flux-to-voltage converter for low frequency magnetic fields. In order to get a view into the functioning of SQUID, we have to apply the rules for describing physics of the micro-world: the quantum mechanics. We need to look at three important facts in physics: superconductivity, quantum tunneling and magnetic flux quantization.

The phenomenon of superconductivity was discovered in 1911 by the Dutch physicist Heike Kamerlingh Onnes (1911). He noticed that mercury shows no electrical resistance when cooled to the temperature of liquid helium (4.2 K). Later on, several other metals and alloys were found to experience the same effect when cooled to very low temperatures. The explanation of this low temperature superconductivity [in opposition to the high temperature conductivity discovered by Karl Alex Mueller and Johannes Georg Bednorz in 1986 (Bednorz and Mueller 1986) and not yet sufficiently explained] came rather late: In 1957, John Bardeen, Leon N. Cooper and J. Robert Schrieffer published the theory (Bardeen et al. 1957) now known as the BCS theory of superconductivity. They have explained superconductivity as a result of the existence of pairs of electrons, now called Cooper pairs, each of which is formed of two electrons of opposite spin and momentum. Hence, the Cooper pair has a zero net spin and zero net momentum. Pairing of electrons is caused

by the attractive force. Behind is an interaction between the negative charge of electrons and the positive charge of the ion cores in the material that is in the superconducting phase. The binding energy of the Cooper pair is very low (in the range of meV), but high enough to prevent each pair from moving apart by scattering. Consequently, pairs of electrons can move through the superconducting material without being affected by opposing forces and superconductive material shows no macroscopic electric resistance. On the other side, single electrons in normal conductors experience several obstacles: lattice vibrations, impurities, defects in crystal lattice. This scattering of electron is macroscopically demonstrated by the electric resistance.

Quantum mechanical description of superconducting current formed by the Cooper pairs requires the knowledge of a wave function. This useful mathematical tool to describe the micro-world of quantum systems is characterized by the amplitude and the phase, similarly as in all forms of waves in physics. Superconductors here also are something special: They need only one wave function to describe all Cooper pairs. If no current flows, all the pairs also have the same phase (they are phase coherent).

After the BCS theory appeared, several calculations followed and in 1962 Brian D. Josephson (Josephson 1962) predicted an effect, now called the Josephson effect. He considered two superconductors separated by a thin layer of an insulating material, which acts as a barrier for the current flow. What will happen with the superconducting current if the current circuit is established (Fig. 9.1)? It is reasonable to expect that the wave function enters the barrier region from both sides of the superconductors, since there are Cooper pairs on both sides of the barrier. If the barrier is thin enough, the wave functions from both sides will overlap. And if the overlap is sufficient over the barrier space, the phases of both wave functions are locked together. Consequently, the Cooper pairs can experience what is called in quantum mechanics tunneling. That means they can penetrate the barrier without breaking up. This kind of Cooper pair tunneling is the Josephson tunneling. The Josephson junction of the two superconductors separated by the insulation barrier acts as some sort of weak superconductor. The maximal supercurrent that flows through this weak superconductor is determined by barrier geometry, material and temperature. Quantitatively, the current through the junction is given

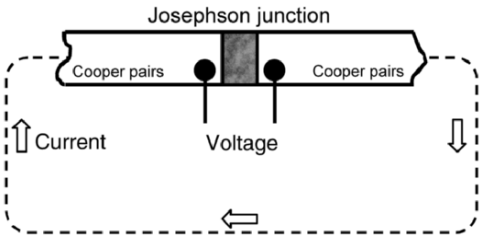

Fig. 9.1. Josephson junction in superconducting circuit

by the first Josephson equation. This effect is called the direct-current (dc) Josephson effect, to distinguish it from the also existing alternating-current (ac) Josephson effect, described by the second Josephson equation.

Josephson junctions have several applications in the superconducting electronics, however their most spread application until now is in SQUIDs.

Before describing SQUID in detail, we have to mention the last fundamental stone: the magnetic flux quantization. This is an example of quantization which is observable in macroscopic dimension. Considering a superconducting ring or a hole in a superconductor, F. London has shown that the fluxoid ϕ', defined as

$$\phi' = \phi + \frac{m^*}{n_s^* e^{*2}} \oint \mathbf{j}_s \cdot d\mathbf{s}, \tag{1}$$

takes only values of integral multiples of the flux quantum $\phi_0 = h/2e = 2.07 \cdot 10^{-15}$ Vs. ϕ is here the outer magnetic flux through the surface encircled by the integration path, $\mathbf{j}_s$ is the supercurrent density, m^*, n_s^*, e^* refer to the mass, density and charge of a Cooper pair. Taking the integration path deeper inside the superconducting ring, we see that there is $\mathbf{j}_s = 0$ and consequently $\phi' = \phi = n\phi_0$, i.e. the flux itself is quantized in such a case. The flux quantization was experimentally demonstrated in 1961 (Deaver and Fairbank 1961).

Today, we use SQUID mainly in the so-called dc-SQUID configuration. Basically, it consists of a superconducting ring interrupted by two Josephson junctions (Fig. 9.2a). To get out of this geometrical configuration sensor, which could be described as a flux-to-voltage converter, we have a) to cool the dc-SQUID to the superconducting state (usually we work with classical superconductors and we cool the dc-SQUID to 4.2 K, to the temperature of liquid helium) and b) we have to send current (mainly of Cooper pairs of electrons) symmetrically through it (Fig. 9.2b). According to that mentioned earlier, the Cooper pairs will tunnel trough both Josephson junctions (weak

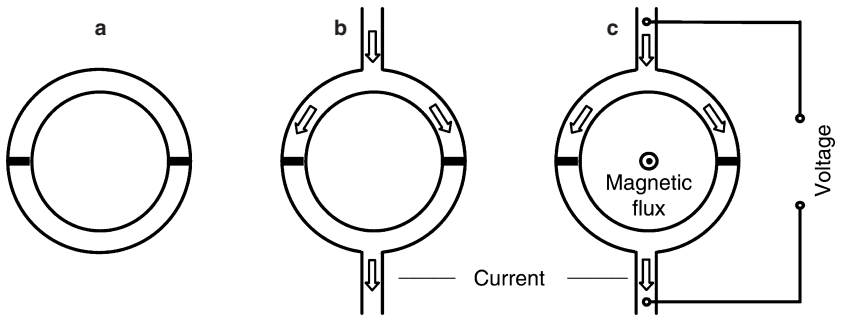

Fig. 9.2. dc-SQUID configuration: **a** superconducting ring with two Josephson junctions, **b** the same with bias current, **c** with magnetic flux threading the ring

links) and afterwards proceed the flow on (Fig. 9.2b). Let us now apply a slowly increasing magnetic field to the dc-SQUID with biased current so that some magnetic flux will thread the ring. This magnetic field will alter the current. Primarily, the quantum mechanical phase difference across each of the two junctions will be changed and consequently the critical current of the SQUID: We will observe that the current will oscillate between the maximal and minimal value as the magnetic flux will increase trough the ring. (The same alteration in current happens if the magnetic flux through the ring decreases.) The current maximum occurs always when the flux trough the ring equals to the integer number of flux quanta ϕ_0. The minimum of current corresponds to the half integer values of ϕ_0. What we measure is not the current, but rather the voltage across the SQUID (Fig. 9.2c). Voltage, which also oscillates between the maximal and minimal values, is more practical for further detection with the commonly used procedure in electronic devices, including the lock-in-amplification and the negative feedback loop technique, so that we finally have a zero balance detector, which enables us to measure 10^{-5} ϕ_0 or better on the linear part of the slope between N and $N+1/2$ ϕ_0. In Fig. 9.3a one can see schematically the current versus voltage dependence for both extreme values of magnetic flux and voltage versus magnetic flux dependence. The pattern in V versus ϕ/ϕ_0 curve (Fig. 9.3b) reminds us to the interference phenomena in waves, as for instance in optics. Therefore the name quantum interference effect. Here we observe the interference of two wave functions describing the events in both Josephson junctions of a dc-SQUID.

Knowing the energy associated with magnetic flux $\left(\frac{1}{2}LI^2\right)$ we can obtain for the SQUIDs of today's production a sensitivity in the order of about 10^{-32} J. That is not far from the limit following from the Heisenberg's uncertainty principle. Obviously, we have to "bring" the measured magnetic field to the SQUID, which is cooled with the liquid He in the cryostat and is also well protected with the superconducting shield (the Meissner effect is exploited). We do that by inductive coupling of the measured magnetic field with the dc-SQUID via the so called flux transformer (Fig. 9.4). We see from Fig. 9.4 that the flux transformer can be in a form of magnetometer or gradiometer of different order. All these input circuits, as they are often called,

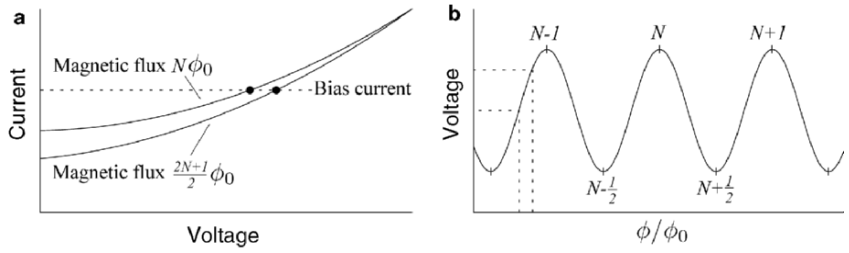

Fig. 9.3. **a** Current vs voltage, **b** voltage vs ϕ/ϕ_0 for dc-SQUID

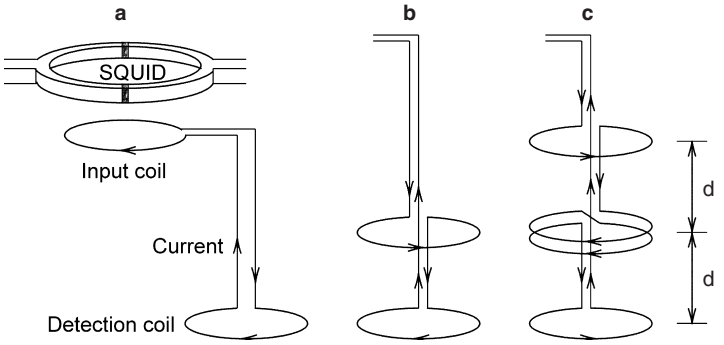

Fig. 9.4. **a** Schematic presentation of flux transformer, which consists of a detection coil (magnetometer) connected with the SQUID's input coil. In noisy environment, the detection coil can be arranged in **b** 1st order gradiometer or **c** 2nd order gradiometer configuration

are built of superconducting material and inductively coupled to the dc-SQUID. Hence, they experience the appearance (or change) of supercurrent if an external magnetic field is present or if it alters. This current causes a flux in the dc-SQUID and we read it as an output signal in terms of a voltage change in SQUID electronics. Because the magnetometer's detection coil is often larger then the dc-SQUID ring, we reach higher final sensitivity. The resolution of a good system is close to 1 fT (1femtotesla=10^{-15} T). The magnetometer input coil is practically applicable only in the extremely well magnetically shielded measuring room (Erné et al. 1981). With the gradiometer configuration, we can further eliminate disturbances and noise if their source is far enough from the two in opposite direction wound coils. Such an extensively disturbing source can be considered as uniform at the point of the two gradiometer coils and its contribution cancels out. The gradiometer of the 2nd order cancels out the homogeneous contribution and the 1st gradient. In practice, we go up to 3rd order gradiometer.

So far, we have described the single dc-SQUID with the proper input circuit and magnetic shielding. Historically, the first SQUID measuring systems were using the radiofrequency field as the biasing source (Zimmerman et al. 1970). This type of SQUD is called the rf-SQUID, and consists of a single Josephson junction in a superconducting ring. The ring is inductively coupled with the coil of an rf oscillator, which forms a resonant circuit. The driving current is the rf current. The voltage across the resonant circuit oscillates when the outer magnetic flux alters. Very few rf-SQUIDs are still in operation. They are less sensitive then the dc-SQUIDs. The production of dc-SQUID is based on the multilayer thin film technology known from microelectronics and it can be done in a high number of samples on a silicon substrate.

During the 40 years (Jaklevic et al. 1964) of SQUIDs history we have seen considerable progress. Until the early 1980s, we were using single channel measuring systems and performing scanning over the area where the magnetic field distribution was later re-constructed offline. In the mid and late 1980s the multichannel devices came in use and they were consisting of more and more SQUIDs built in the system (4, 7, . . . 37) (Koch et al. 1991). The new combinations included the electronic design of gradiometers in different parallel planes (Drung 1995) and also spatial 3D orientation of some magnetometers. This provides real 3D information by using all three components of the measured magnetic field vector (Kotani et al. 1997).

One sector of SQUID development in the recent years went towards construction of SQUID systems (usually one channel) with the highest spatial resolution. Sometimes the expression SQUID-microscope (Baudenbacher et al. 2002) is used for these devices. While large multichannel SQUID measuring system covers with their detection coils an area of several 10 cm^2, a high spatial resolution SQUID system covers a surface of 1/4 mm^2 or less. In order to best exploit this small area of detecting coil, it has to be brought as close as possible (maybe a few 100 μm) to the plane of measurement. This is a severe technical problem, since the detection coil is in the superconducting state.

The high temperature superconductors are also the "raw" materials for the high T_c SQUIDs. Soon after the discovery of the high temperature superconducting material $YBa_2Cu_3O_{7-\delta}$, also called YBCO (yttrium barium copper oxide), with $\delta \sim 0.15$ and with the transition temperature close to 90 K, it was possible to manufacture good SQUIDs. This ceramic material is suitable to be deposited in form of a thin film using the laser deposition technique. The YBCO thin film is epitaxially grown on a substrate.

YBCO SQUIDs were constructed in different geometrics and they need a suitable flux transformer for better sensitivity. They reach a white noise level of some 20–30 f $T/Hz^{1/2}$. They operate at liquid nitrogen (77 K) and this is an advantage when liquid helium is difficult to purchase for some reason. However, the high temperature SQUIDs will never reach the resolution of their low temperature predecessors due to different kT (k is the Boltzmann constant, T is the absolute temperature of cooling medium 77 K and 4 K). They will be used in applications where the highest sensitivity and resolution is not essential.

9.3 Basic steps in analysis and modeling of sources of electric activity connected to electric and magnetic measurements

There are different approaches to model bioelectric phenomena. They range from single cell events to complex macroscopic electric and/or magnetic measurements on, for instance, parts of the human body or electric events in

particular electrically active organ. We will briefly mention the principles and later, apply some of them to measurements on plant cells and to parts of a plant.

9.3.1 Direct and inverse problem

Knowing the bioelectric current source(s) and the electrical properties of the tissue around an electrically active organ, we can calculate the electric potential on some surface encircling (embodying) this organ at some distance. This type of calculation is known as a direct problem (Plonsey 1969). The direct problem has always a unique solution, i.e. a given distribution of currents in an electrically active organ leads to one and only one surface distribution of electric potential. The calculation is based on the second Green's theorem (Stratton 1941) and requires in three-dimensional geometry numerical integration and implication of standard methods like the boundary element method (Brebbia et al. 1984) and the finite element method (Burnett 1987). As an illustration we may mention the probably most known direct problem—the human heart and the electric potential on the torso (Barr et al. 1977). The potential on the human torso is connected to the potential distribution on the surface of the heart (epicardium)

$$\Phi_T = \mathbf{Z}_{TE}\Phi_E. \tag{2}$$

Here is $\Phi_T = \left(\Phi_T^1, \Phi_T^2, \ldots \Phi_T^{N_T}\right)$ a vector formed by discrete values of potential in N_T points, $\Phi_E = \left(\Phi_E^1, \Phi_E^2, \ldots \Phi_E^{N_E}\right)$ is a vector formed with the potentials values in N_E points on the epicardial surface and $\mathbf{Z}_{TE}$ is a matrix of geometric coefficients with the $(N_T \times N_E)$ dimension.

Eq. (2) enables us to calculate the potential on the torso surface from the known distribution of potentials over the epicardium, provided that we know the matrix $\mathbf{Z}_{TE}$. This is the case in studies of animal subjects where we measure the potential on the epicardium (Ramsey et al. 1977). In human subjects we measure the potential distribution in points (up to 200) on the torso surface and we calculate the potential distribution over the epicardium. That means that we have to solve the inverse problem. We can represent it in a similar way as the direct problem

$$\Phi_E = \mathbf{Z}_{ET}\Phi_T. \tag{3}$$

Here is $\mathbf{Z}_{ET}$ matrix of geometric coefficients with the $(N_E \times N_T)$ dimension. The $\mathbf{Z}_{ET}$ matrix determines the relation between $\mathbf{\Phi}_E$ and $\mathbf{\Phi}_T$. It has to be noticed that the inverse problem is an ill-posed problem. The number of linear independent solutions is smaller in comparison to the number of unknowns. Special care must be taken to assure that we chose a proper solution of the inverse problem (Hansen 1992).

9.3.2 Single cylindrically shaped cell [core (volume) conductor model]

The research of a long single cell is to a good approximation a one-dimensional case. As a consequence, several analytical solutions are possible. Historically, first a mathematical evaluation for the core conductor model (Clark and Plonsey 1966) was obtained. Later the extension towards the calculation of magnetic field for a single axon (Woosley et al. 1985) was completed. Similar calculations for the internodal cell of *Chara corallina* were done (Slibar et al. 2000). In all three mentioned works, the calculation starts with the evaluation of the electric potential from the Laplace's equation

$$\Delta\Phi = 0 \tag{4}$$

with the boundary conditions: the transmembrane potential Φ_m is equal to the difference of intracellular Φ_i and extracellular potential Φ_e: $\Phi_m(z) = \Phi_i(a,z) - \Phi_e(a,z)$, and the normal component of current density at the membrane surface is continuous: $\mathbf{n}\cdot\mathbf{J}_i(a,z) = \mathbf{n}\cdot\mathbf{J}_e(a,z)$. Here $\mathbf{n}$ is normal to the membrane surface; $\mathbf{J}_i$ and $\mathbf{J}_e$ are intracellular and extracellular current densities, respectively. The meaning of all quantities is evident from Figs. 9.5 and 9.10 For Φ_i and Φ_e the following expressions were obtained (Clark and Plonsey 1966)

$$\Phi_i(\rho,z) = \frac{1}{2\pi}\int_{-\infty}^{\infty}\frac{I_0(|k|\rho)}{\beta(|k|a)I_0(|k|a)}\varphi_m(k)e^{-ikz}dk, \tag{5}$$

$$\Phi_e(\rho,z) = \frac{1}{2\pi}\int_{-\infty}^{\infty}\frac{K_0(|k|\rho)}{\alpha(|k|a)K_0(|k|a)}\varphi_m(k)e^{-ikz}dk. \tag{6}$$

Here are $\alpha(|k|a) = -\left[1+\gamma(|k|a)\right]$, $\beta(|k|a) = 1+\dfrac{1}{\gamma(|k|a)}$,

$\gamma(|k|a) = \dfrac{\sigma_e K_1(|k|a)I_0(|k|a)}{\sigma_i K_0(|k|a)I_1(|k|a)}$. I_0, I_1, K_1 and K_1 are the modified Bessel functions, and $\varphi_m(k)$ is the spatial Fourier transform of the transmembrane potential

$$\varphi_m(k) = \int_{-\infty}^{\infty}\Phi_m(z)e^{ikz}dz. \tag{7}$$

Combining Eqs. 5–7, the following connections were obtained (Woosley et al. 1985)

$$\varphi_i(\rho,k) = \frac{I_0(|k|\rho)}{\beta(|k|a)I_0(|k|a)}\varphi_m(k), \tag{8}$$

$$\varphi_e(\rho,k) = \frac{K_0(|k|\rho)}{\alpha(|k|a)K_0(|k|a)}\varphi_m(k). \tag{9}$$

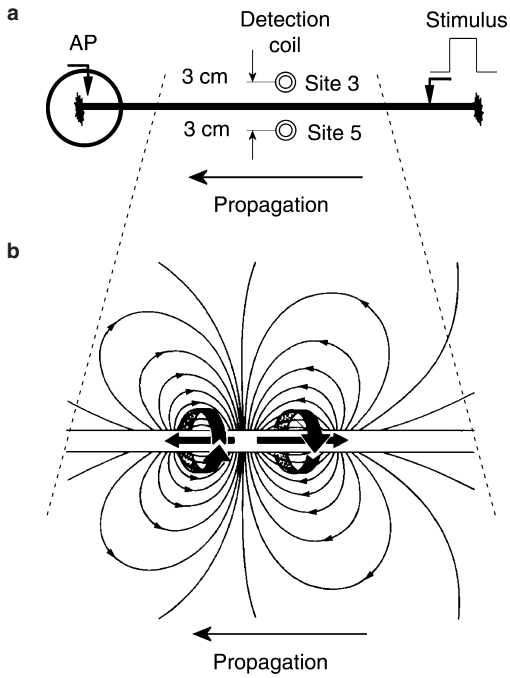

Fig. 9.5. **a** Schematic of *Chara corallina* internodal cell (*top view*) indicating the location of the stimulus, the AP and the magnetic field measurement sites. **b** Schematic distribution of intracellular current (two current dipoles within the internodal cell) and extracellular current (thin lines) for a propagating AP along the *Chara corallina* internodal cell. The contribution of the extracellular current to the measured magnetic field is negligible in an extended bath. The magnetic field due to the intracellular current in the vicinity of the internodal cell is represented as a ring around the cell. The depolarized part of the cell is shown on the left side, the repolarised on the right side

They also calculated the magnetic field B_i due to the intracellular current density by applying the law of Biot-Savart or Ampère

$$B_i(\rho,z) = \int_{-\infty}^{\infty} G(\rho,a,z-z')J_i^z(a,z')dz. \tag{10}$$

Here J_i^z is the intracellular current density component along the cell and G is the Green function of a ring around the membrane at z′

$$G(\rho,a,z-z') = \frac{\mu_0}{4\pi}\int_{-\pi}^{\pi} \frac{a}{\sqrt{\rho^2+a^2-2a\rho\cos\vartheta+(z-z')^2}}\,d\vartheta, \tag{11}$$

In the k-space, the connection with the $\varphi_m(k)$ was obtained

$$b_i(\rho,k) = i\mu_0 a\sigma_i k \frac{I_1(|k|a)K_1(|k|\rho)}{\beta(|k|a)}\varphi_m(k). \tag{12}$$

They added results for $B_e(\rho,z)$ and $b_e(\rho,k)$ due to the extracellular current density. The total magnetic field was obtained by summing $b_i(\rho,k)+b_e(\rho,k) = b(\rho,k)$. With the Fourier transformation we obtain magnetic field $B(\rho,k)$. The path of calculations can be presented as

$$\Phi_m(z) \underset{F^{-1}}{\overset{F}{\rightleftharpoons}} \varphi_m(k) \rightleftharpoons b(\rho,k) \underset{F}{\overset{F^{-1}}{\rightleftharpoons}} B(\rho,z), \tag{13}$$

where F and F^{-1} denote the Fourier and inverse Fourier transformations, respectively. Applications of these calculations to the internodal cell of *Chara corallina* will be shown in section 9.4.

9.3.3 Covariance method—dc fields

The covariance method turned out to be suitable in extracting the dc component of the modulated magnetic field data. This is important in studies of electric response to injury (Curio et al. 1993; Wübbeler et al. 1998). The covariance of the discrete measured magnetic signal (B^k) and the modulation signal (m) during n periods of modulation signal is by the definition

$$\operatorname{cov}\left(B^k, m\right) = \frac{1}{N}\sum_{i=1}^{N}\left(B_i^k - \overline{B}^k\right)\left(m_i - \overline{m}\right) = \frac{1}{2}A\left(B^k\right)M. \tag{14}$$

Here $N=nf_s/f_m$ is the number of measured points in the given time interval, f_s is a sampling frequency and f_m is a modulation frequency. $\overline{B}^k$ and $\overline{m}$ are the mean values of B^k and m. The modulation amplitude is

$$M = \sqrt{2\operatorname{cov}(m,m)} \tag{15}$$

The response of the measured subject follows from eqs (14) and (15) as

$$A\left(B^k\right) = \sqrt{\frac{2}{N}}\frac{\sum_{i=1}^{N}\left(B_i^k - \overline{B}^k\right)\left(m_i - \overline{m}\right)}{\sum_{i=1}^{N}\left(m_i - \overline{m}\right)^2}. \tag{16}$$

9.3.4 Current distribution with the minimum norm estimation

This is a method that can also be used in solving the inverse problem. This means that we can limit the space where to reconstruct the current sources and then search for the suitable current distribution based on the estimation of the minimal norm in the distribution of primary currents (Parker 1977; Sarvas 1987).

Magnetic field (B_i) at the position ($\mathbf{r}$) of the i-th detector ($\mathbf{e}_i$-unit vector corresponded to the direction of the measured magnetic field) and the current caused by a primary current source ($\mathbf{j}_p$) in an infinite homogeneous medium, may be obtained from the Biot-Savart law as

$$B_i = \mathbf{B}(\mathbf{r}) \cdot \mathbf{e}_i = \frac{\mu_0}{4\pi} \int_V \frac{\mathbf{j}_p \times (\mathbf{r} - \mathbf{r}') \cdot \mathbf{e}_i}{|\mathbf{r} - \mathbf{r}'|^3} dV'. \tag{17}$$

This field can be rewritten in the form

$$B_i = \int_V \mathbf{L}_i(\mathbf{r}') \cdot \mathbf{j}_p(\mathbf{r}') \, dV' = \langle \mathbf{L}_i, \mathbf{j}_p \rangle, \tag{18}$$

where $\langle \mathrm{L}_i, \mathrm{j}_p \rangle$ denotes a dot product in a linear functional space ***J*** of all primary current sources and $\mathbf{L}_i$ is the so-called lead function of the i-th detector

$$\mathbf{L}_\mathrm{i}(\mathbf{r}') = \frac{\mu_0}{4\pi} \frac{(\mathbf{r} - \mathbf{r}') \times \mathbf{e}_\mathrm{i}}{|\mathbf{r} - \mathbf{r}'|^3}. \tag{19}$$

Lead function $\mathbf{L}_i$ represents transfer between the unit current dipole in **r'** and the measured magnetic field B_i in **r**. The current source $\mathbf{j}^*$ in ***J***, which can explain the measured magnetic field, is obtained as linear combination of lead functions

$$\mathbf{j}^*(\mathbf{r}') = \sum_{k=1}^{N} w_k \mathbf{L}_k(\mathbf{r}'), \tag{20}$$

where *N* is number of magnetic field detectors. Eqs (18) and (20) lead to a system of linear equations

$$B_i = \sum_{k=1}^{N} w_k \langle \mathbf{L}_i, \mathbf{L}_k \rangle = \sum_{k=1}^{N} \Gamma_{ik} w_k, \, i = 1, 2, \ldots N. \tag{21}$$

If we suppose that the inverse of the lead matrix Γ exists, then the solution of Eq. (21) is

$$\mathbf{W} = \left(w_1, w_1, \ldots w_N\right)^T = \Gamma^{-1}\left(B_1, B_2, \ldots B_N\right)^T = \Gamma^{-1}\mathbf{B}. \tag{22}$$

The solution $\mathbf{j}^*$ in Eq. (22) is an orthogonal projection of the primary currents in subspace in ***J***, determined by the lead functions. It has consequently the minimum norm out of all possible current distributions ($\mathbf{j}' \in \boldsymbol{J}$), which solve Eq. (20); this gave the name to the present method (Sarvas 1987). The conditions for the existence of a solution in Eq. (22) can be further proven. However, it has to be mentioned here that all difficulties inherent to the inverse problem appear also in this method. One has to know, for instance from the physiological information, where/when the current distribution is relevant, in order to exclude non-relevant current distributions (Hämäläinen and Ilmoniemi 1994).

9.4 Case studies

Methods and models mentioned in sections 9.2 and 9.3 were also applied to the world of plants. In the following we present, to some extent historically, a few magneto- and electrophysiologic experiments in plants.

To illustrate magnetic studies on electrophysiology in plants it is suitable to start in analogy to the research on signal transmission in simple excitable systems like the giant squid axon (Wikswo et al. 1980) and the peripheral nerve (Trahms et al. 1989). The ideal candidate for this is obviously the internodal cell of the green algae *Chara corallina*.

Electrophysiologic research on electrical phenomena on internodal cells of the giant green algae the *Characeae* started already in 1929 (Umrath 1929) and was extensively followed by others (Hope and Findlay 1964; Hope and Walker 1975) until now. Experimental work was certainly favored by the dimensions of the *Characeae* internodal cells; they can be as long as 10 cm with a diameter of about 1 mm. Any manipulation and microsurgery of such cells was successful (e.g. Beilby 1990; Shimmen et al. 1994). Because of its simple geometry, its electrical excitability and because of the huge body of work done on these cells it is justified to say that the species *Chara corallina* is the plant equivalent to the squid axon when studying ion transport in plants.

Already in the late 1970s, Frank Blatt from the University of Michigan had started the first measurements on magnetic field changes related to electrical activity in *Chara*. However, this had to wait some more years and improvement of SQUID sensors to successfully record magnetic equivalent signals to electric measurements in *Chara* (Trontelj et al. 1994). In the following, we shall mainly stay with SQUID measurements of magnetic field caused by ionic currents in electrically excited internodal cell of *Chara corallina*. Magnetic measurements will almost always be shown in parallel with electric measurements; the latter were conducted with a technique that does not disturb the SQUID sensor(s). Multichannel SQUID measurements and high spatial resolution SQUID measurements will be used.

9.4.1 Measurements of action current (AC)—magnetic analogy to action potential (AP) in *Chara corallina* using the multichannel SQUID measuring system

It seems to be a very obvious idea to measure the magnetic field or a component of it in the vicinity of a cell; in this way it is possible to obtain the value of the intracellular ionic current in the internodal cell of *Chara corallina* from measurements of AP (see chapter 2 in this book). Ampère's law gives easy first magnetic field estimation, assuming that we are so close to the cell that the excited length of the internodal cell is much longer than the distance from the cell to the sensor. Taking for the intracellular axial current I=1 μA we obtain for d=1 mm away from the cell surface $B=\mu_0 I/2\pi r$ 10^{-10} T=100 pT. This is a measurable magnetic field but only if the SQUID input coil is not more than a 1 mm away from the *Chara corallina* internodal cell. Such a close positioning can be achieved only with the high spatial resolution set-up (SQUID microscope). In the multichannel SQUID system within the Dewar vessel of about 30 cm diameter, a distance from the SQUID detection coil to the cell is at least 3–5 cm. With this arrangement the signal is reduced due to

(i) the increased distance and (ii) due to the fact that in this case the current source in form of a current dipole has to be considered. The total estimated reduction is 2 orders of magnitude, i.e. we have at the detection coil only 1 pT. Figure 9.5 shows the geometry (schematically) of a *Chara corallina* cell and the positions of two out of 37 detection coils. The drawing also illustrates the position for the AP measurement, and the site of stimulation. Finally the drawing shows the positions of the current dipole, which cause the depolarizing and repolarizing AC with the corresponding volume currents and indication of the corresponding magnetic field. Such a measuring condition requires a very good magnetic shielding and carefully prepared measurement, since we cannot count on averaging to improve the signal/noise ratio. Successful measurement were done (Trontelj et al. 1994) in the Berlin magnetically shielded room (Erné et al. 1981) and here are some experimental details: A single *Chara corallina* internodal cell was isolated from the adjacent cells and placed in artificial pond water (APW) for 1 or 2 days before being used in experiments. One end of the internodal cell was mounted into a Plexiglas support (Fig. 9.6), which allowed electrical isolation of this end by means of a groove containing grease; note the junction between the APW and KCl compartment in Fig. 9.6. The internodal cell was inserted in a horizontal Plexiglas tube with large holes in the wall. The size off each hole was ~20 mm × 5 mm and all together constituted more than 50% of the Plexiglas tube surface. Such large holes are necessary to provide undisturbed circulation of the return (volume) current. The Plexiglas support together with the *Chara* corallina internodal cell was then submerged in a Petri dish of 220 mm inner diameter. Recording of the action potential was similar to that described previously (Moriyasu et al. 1984; Clint and MacRobbie 1987). Briefly, the

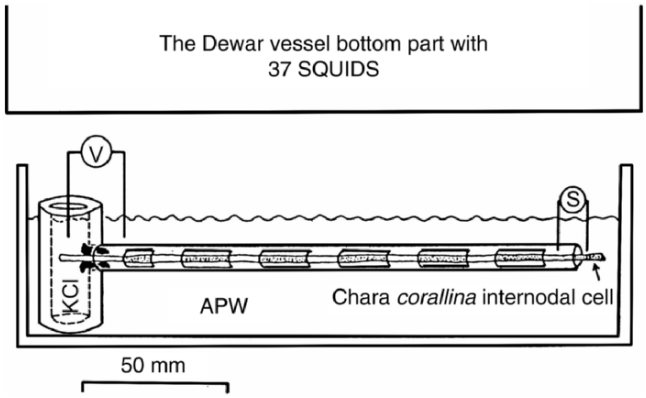

Fig. 9.6. Schematic representation of recording configuration. Magnetic recording of the action potential was carried out by 37 dc-SQUID magnetometers mounted in a cryostat filled with liquid helium and positioned above the *Chara corallina* internodal cell. The distance between the plane containing SQUID magnetometers and the cell was 50 mm

Plexiglas support compartment was filled with 100 mM KCl. This compartment served as the reference point for electrical measurements by a voltage follower. Suprathreshold stimulation was obtained by a pulse generator. The measurement set-up for electric potential measurements has a bandwidth dc −50 Hz. Ag/AgCl electrodes were used and resting potential was determined as the potential difference between the APW and KCl compartment. Internodal cells of 140–210 mm length and about 1 mm diameter were selected. With a 120-s stimulation period, some cells were responsive to several tens of stimulations.

The magnetic field was measured simultaneously at 37 points on a horizontal plane 50 mm above the *Chara corallin*a internodal cell with a multichannel magnetometer system consisting of 37 dc-SQUID magnetometers. Each of them had a 50 mm^2 pick-up coil area and 0.016–250 Hz band width (Fig. 9.6) (Koch et al. 1991).

Figure 9.7a,b show the time evolution of two characteristic magnetic signals (vertical components from channels 3 and 5) out of 37 signals. The detection coils nos. 3 and 5 are positioned on different sides of the *Chara corallina* internodal cell (see numbers in Fig. 9.7c). Hence an inverse polarity of both signals has to be expected. Also there is no signal detected in all detection coils (for instance, coils 0, 1, 4) just above the internodal cell. In this case the magnetic field lines are parallel to the plane of the detection coil and contribute zero to magnetic flux through the detection coil. With this

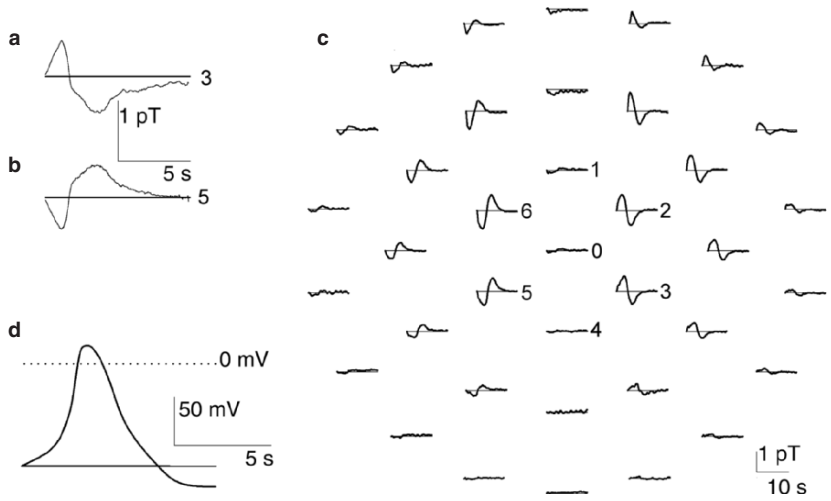

Fig. 9.7. **a** The time evolution of magnetic field measured with the detection coil no. 3 and **b** the same, only the detection coil no. 5 is on the opposite site of the cell. **c** The time evolution of magnetic field (vertical component) in 37 points in a plane 50 mm above Chara corallina internodal cell. The signal amplitude just above the cell, place in the middle of the figure extending top to bottom, is practically 0, as is expected for the current dipole travelling along the cell. **d** The time evolution of action potential. The first 10 s are shown

information in mind, the picture of all 37 magnetic channels simultaneously measured (Fig. 9.7c) becomes understandable. The time evolution of the corresponding electrically measured AP is shown on Fig. 9.7d. With the information presented in Fig. 9.7c we can also obtain after an interpolation procedure the isofield representation for a particular time. Results for three consecutive time points are presented in Fig. 9.8. They indicate a vertical component of the magnetic field values. The time between two representations is 300 ms. The dipolar distribution of the magnetic field suggests that the current generator behaves similar to that of animal cells, and the spatial co-ordinates of the central part of the intracellular current distribution can be estimated. Close inspection of Fig. 9.8 also indicates the motion of excitation along the cell. The projection of the stimulus location corresponds to the point in the central upper part of each image in Fig. 9.8. The excitation is spreading from top to bottom in each picture. The time increases from left to right. By comparing the position of the magnetic field extrema, indicated by the + and − signs, this propagation can be followed as a shift in position of both extrema in time. By evaluating the movement of the extrema per unit time, we obtained a speed for excitation propagation of 3–5 cm/s. This value is in agreement with values for excitation propagation in *Chara* obtained by different groups (Findlay and Hoppe 1976; Tester 1990).

Another choice of time intervals after the cell's excitation and between isofield representations enables us to demonstrate the depolarization and the repolarization phase in the same sequence of pictures. This is demonstrated in the first row of Fig. 9.9a–c. The second and the third rows in Fig. 9.9a–c show the calculated equivalent current dipoles (central row) and the current distribution (bottom row) along the *Chara corallina* internodal cell. The calculation was based on the estimation of minimal norm (see Section 9.3.4) in the distribution of equivalent intracellular currents according to Eqs 17–22 in section 9.3.4.

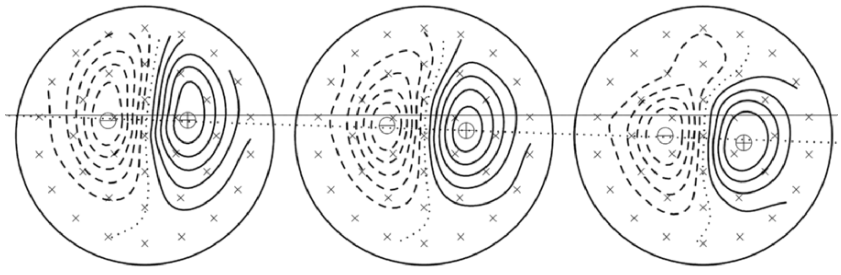

Fig. 9.8. The isofield line representation at three particular times, from left to right at 1300 ms, 1600 ms and 1900 ms after the stimulus. The solid line (a reference) and the *dotted line* lead the eyes to follow the displaced extrema as it explained in the text. The *crosses* indicate the points where magnetic field was measured. They are arranged in three concentric circles with radii of 3.5, 7, and 10.5 cm. The two neighboring isofield lines are 150 f T apart

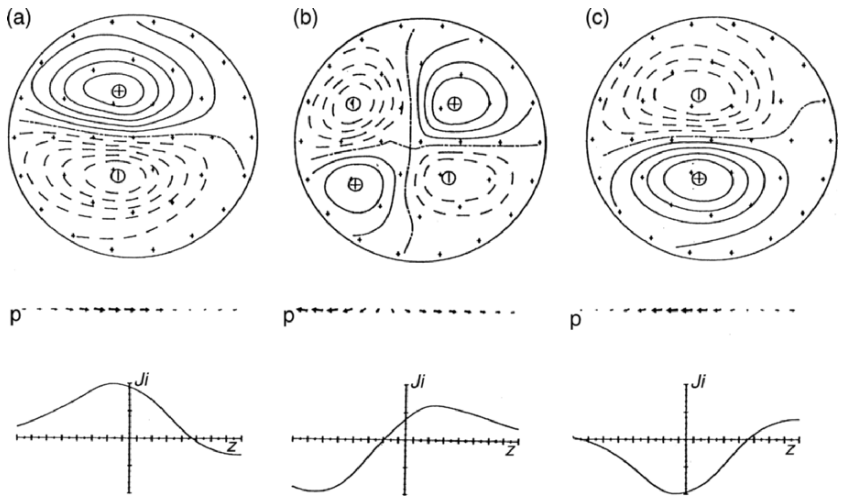

Fig. 9.9. The isofield representation (*first row*), and the model calculation of current dipoles (**p**, *second row*) and current density (J_i, *third row*) along the cell for: (a) the depolarization, (b) depolarization+repolarization, and (c) repolarization at times 1.4, 2.5 and 3.6 s after stimulus

The *Chara corallina* internodal cell offers a convenient model system to test calculations (Clark and Plonsey 1966; Woosley et al. 1985; Slibar et al. 2000) of relations between intracellular current, magnetic field and electric potential. The respective calculations are briefly mentioned in section 9.3.2 (Eqs. 5–13). Considering the cylindrical symmetry of *Chara corallina* internodal cells we represent this cell geometrically according to Fig. 9.10. Transformations from measured the AP→the calculated AC (magnetic field)

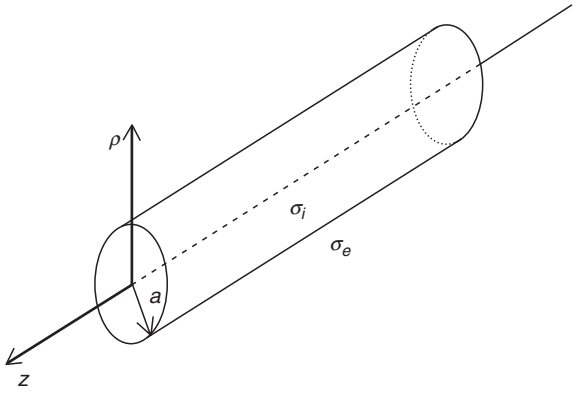

Fig. 9.10. The cell model. σ =1.2 $\Omega^{-1}m^{-1}$, σ_e=0.025 $\Omega^{-1}m^{-1}$, and 2a=1 mm

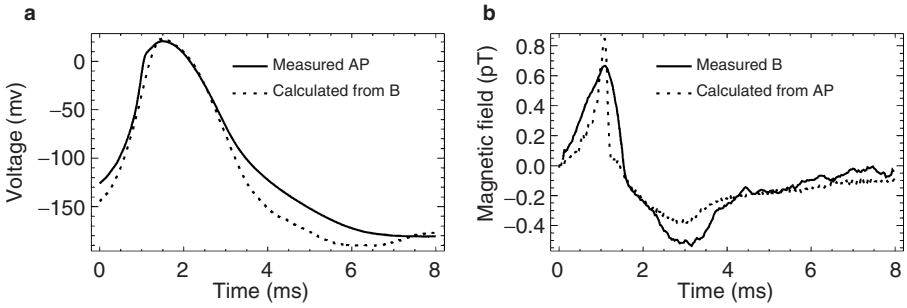

Fig. 9.11. **a** The first 8 s of measured AP (*solid line*) in the *Chara corallina* internodal cell and calculated AP (*dashed line*) from the measured magnetic field. **b** Measured magnetic field 6 cm away from the *Chara corallina* internodal cell (*solid line*) and calculated magnetic field (*dashed line*) from the measured AP

and the inverse process from the measured AC (magnetic field)→the calculated AP are presented in Fig. 9.11. Comparisons of all calculations (Clark and Plonsey 1966; Woosley et al. 1985; Slibar et al. 2000) with experimental data show that the peak forward AC (magnetic field) occurs approximately simultaneously with the maximum time derivative of the AP. The maximum backward AC coincides with the most rapid change of the AP during the repolarization. The time of the peak AP corresponds to the zero-crossing between the forward and backward phases of the AC. Here adjustments in time scale have to be considered if the AP and AC were not measured at the same position. On the other hand, there are also differences in the shape of the signals. The internodal cell of *Chara corallina* was submersed up to 10 mm into APW. We did not like to have it deeper, since the distance between the cell and the detection coil should be as short as possible in order to have better signal/noise ratios. Hence within the cell and 5 mm around the cell we have completely fulfilled the condition for the assumed cylindrical symmetry. On the upper part of the internodal cell it may be that the volume currents partly modify the integral magnetic field, i.e. the field that we measure. At the same time there is no such effect to be expected when measuring AP.

9.4.2 The chemical nature of the AP in *Chara corallina* as it can be seen from the non-invasive observation (by SQUID microscope) of the intracellular current under the influence of light

Though we still do not understand in all details the process of electrical stimulation of the AP in *Chara corallina* there is no doubt that a rise in cytoplasmic Ca^{2+} plays a dominant role (Williamson and Ashley 1982; Kikuyama and Tazawa 1983; Wacke and Thiel 2001). This rise in Ca^{2+} is believed to activate Ca^{2+}-sensitive Cl^- channels (Okihara et al. 1991; Homann and Thiel 1994) and

with that generate the depolarization. The activation of K^+ channels supports the repolarization (Thiel et al. 1997).

According to some authors Ca^{2+} enters the cytoplasm via voltage-dependent channels (Tazawa and Kikuyama 2003; Berestovsky and Kataev 2005). On the other hand, investigations have revealed that the threshold for excitation is posed by a quasi all-or-none type liberation of Ca^{2+} from internal stores (Wacke and Thiel 2001; Wacke et al. 2003). In this sense, the AP in *Chara* occurs not to function like a classical Hodgkin Huxley (HH) type AP. This means that the AP is not entirely based on the time and voltage dependent activation properties of plasma membrane ion channels but on a complex signal transduction cascade (Wacke et al. 2003). Similar mechanisms of membrane excitation, which are based on Ca^{2+} release from internal stores, are also well known from animal cells where they are found in muscles (Nelson et al. 1995) and even some neurons (Chavis et al. 1996).

The latter type of a "chemical" action potential was in the past well described by models, which include a non linear dynamic interplay of cytosolic Ca^{2+} ($[Ca^{2+}]_c$) and second messenger stimulated release of Ca^{2+} from internal stores (Othmer 1997). The same modeling approach was also suitable to simulate a large spectrum of phenomena related to membrane excitation in *Chara* (Wacke et al. 2003). One parameter in this model, which is predicted to effect the kinetics of Ca^{2+} mobilization and hence the kinetics, is the cytoplasmic concentration of Ca^{2+} prior to stimulation.

To further test the validity of the model, we examined the kinetics of the AP under conditions in which $[Ca^{2+}]_c$ is altered. This was done by transferring the plants from the dark into the light, because it is known that $[Ca^{2+}]_c$ is in these cells reduced under the influence of light (Miller and Sanders 1987; Plieth et al. 1998). The high spatial resolution SQUID measuring system (SQUID microscope) was used for non-invasive magnetic measurements of AC. Measurements were done in the laboratory of John P. Wikswo at the Department of Physics and Astronomy, Vanderbilt University, Nashville, Tenn., USA (Baudenbacher et al. 2005).

9.4.2.1 Experimental

The internodal cell was held in a horizontal Plexiglas half-tube, similar to that described in section 9.4.1; it is schematically shown in Fig. 9.12. The leveling stage allowed the bath to be moved up and down to adjust the distance between the cell and the tail of the SQUID microscope Dewar vessel. A 10 μm thick Mylar film prevented contact between the cell and the SQUID microscope sapphire window and stabilized the position of the internodal *Chara corallina* cell during scanning. One end of the internodal cell was mounted in a small Plexiglas compartment in order to electrically isolate this end of the cell (the left end in Fig. 9.12) from the bath with a petroleum jelly seal (Fig. 9.12), similarly as in the experiment in section 9.4.1. *Chara corallina*

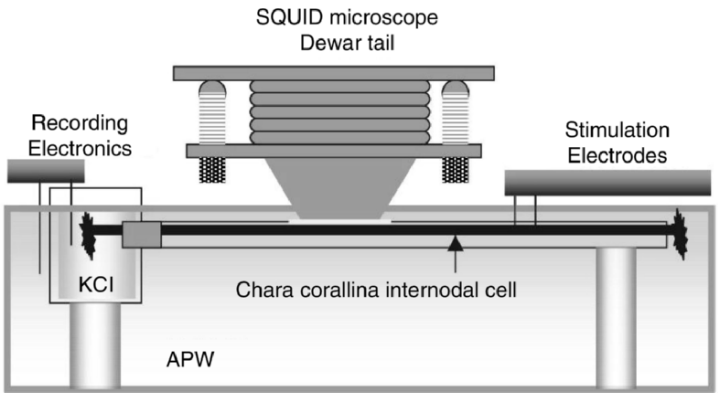

Fig. 9.12. Schematic experimental setup (*side view*) used for electric and magnetic measurements on *Chara corallina* internodal cell. The Plexiglas holder supporting the cell is terminated on the left side in a sealed compartment to record the transmembrane potential

internodal cells were at least 8 cm long to allow simultaneous measurement of the electric potential differences (AP) and the associated magnetic field due to action currents (AC). For the measurements reported here, selected internodal cells were up to 15 cm long with diameters between 0.8 and 1.1 mm.

The bath temperature was carefully monitored during each experiment and was maintained at 20 °C. All measurements were performed in an air-conditioned, magnetically shielded room (Vacuumschmelze, Hanau, Germany). During an average two-hour measuring session, the temperature varied by only 0.20 °C.

The cell illumination was provided by a light source with a spectrum similar to daylight with 5–10 Wm^{-2} delivered to the cell by a fibre-optic bundle that passed through an opening into the magnetically shielded room to eliminate power supply noise of the light source.

By measuring magnetic fields in the vicinity of a *Chara corallina* internodal cell after the AP was electrically elicited, we basically measure the contribution of total ionic current, associated with the propagating action potential (AP). The measured *Chara corallina* internodal cell is in APW bath solution and extracellular ionic currents, caused by the AP propagation along the cell, are spread through the whole APW volume. Their density is very small and their contribution to the measured magnetic field is negligible. In practice, only the magnetic field due to axial intracellular current, the so-called action current (AC), will be measured. To measure it a single SQUID magnetometer was chosen. Its small detection coil can be positioned extremely close to the measured object—SQUID microscope (Baudenbacher et al. 2002). With this configuration, it was possible to obtain a high signal-to-noise ratio (small distance from detection coil to the cell) and high spatial resolution (due to small diameter of detection coil).

In this SQUID microscope design, a hand wound niobium detection coil is coupled to a commercially available low temperature SQUID sensor. The SQUID sensor and the detection coil are in the vacuum space of the cryostat separated typically by approximately 100 µm from the room-temperature sample by a thin sapphire window. A computerized non-magnetic scanning stage with sub-micron resolution in combination with a tripod leveling system allows samples to be scanned at levels of 10 µm below the sapphire window. For a 20 turn, 500 fm diameter detection coil a field sensitivity of 350 $fT/Hz^{1/2}$ was achieved. For a large 40 turn 1 mm diameter coil 50 $fT/Hz^{1/2}$ for frequencies above 1 Hz for the vertical component of the magnetic field was obtained. The voltage output of the SQUID electronics corresponding to the vertical magnetic field component generated by propagating AC was recorded at a bandwidth of DC-500 Hz for a period of 30 s at a position along the cell where the magnetic signal was maximal.

There are some understandable differences in recorded results obtained with the multichannel SQUID magnetometer (Fig. 9.7a–c) and the SQUID microscope (Fig. 9.13a, b). These differences are the result of different distances between the detection coil and the *Chara corallina* internodal cell

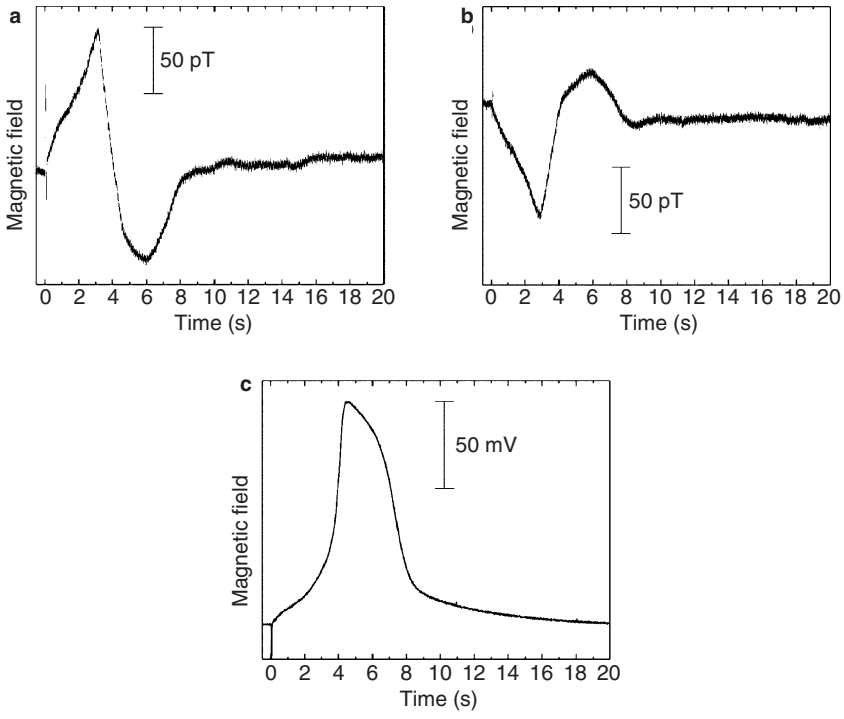

Fig. 9.13. **a** Magnetic field measured at the right side of *Chara corallina* internodal cell and **b** the same at the left side; **c** AP recorded by the K^+ anaesthesia technique

(5 cm for the multichannel SQUID magnetometer and about 200 μm for the SQUID microscope). The amplitude of the vertical component of the measured magnetic field is about 100 times bigger for the single channel SQUID microscope. Since the 500 μm diameter detection coil is so close to the cell, we can say that we are practically observing the linear intracellular ionic current with no influence of a few cm long current dipole. Small differences in peak amplitudes between Fig. 9.13 a and b reflect scattering between two measuring sessions; possibly also small deviation from symmetrically located measuring points contribute to these differences.

The AP was measured simultaneously at a point along the cell 50 mm away from the detection coil position and is shown in Fig. 9.13c. The spatial separation of magnetic and electric measuring points leads to a time shift of 1.1–1.2 s. From these values, the AP propagation velocity can be calculated to be about 4 cm/s, which is in good agreement with the previously mentioned results (section 9.4.1). Before and during these measurements, the *Chara corallina* internodal cell was kept in darkness for at least one hour. The detection coil was placed 2 mm right (Fig. 9.13a) and 2 mm left (Fig. 9.13b) lateral to the internodal cell surface. The vertical distance from the detection coil to the cell surface was 200 μm. The measurements shown in Fig. 9.13 are single shot measurement with no averaging of the data.

Under constant illumination and temperature, the transmembrane potential and the magnetic field generated by AC revealed only small variations either when different cells or when one *Chara corallina* internodal cell was measured repetitively.

Figure 9.14 left panel, traces a–i show the time dependence of the vertical component of the magnetic field measured at y=2 mm lateral to the cell's geometrical axis under different illumination conditions. In this series of experiments, the internodal cell was in darkness for 60 min prior to the first measurement of AP propagation. Figure 9.14, left panel, trace a shows the magnetic field generated by AC just before the light was turned on. Subsequent recordings were done under constant illumination after particular time intervals as shown in Fig. 9.14, left panel, traces b–e. It can be seen that, as a response to illumination, the temporal evolution of the magnetic field changes over a period of less than 1 hour before reaching a new steady state. Most pronounced is the time shift of the positive peak of the magnetic signal associated with the depolarization. The negative peak associated with the repolarization is less expressed.

The temporal characteristic of the magnetic field is reversible. Upon transferring the cell back from light into darkness, the temporal field changes became progressively closer to the initially measured magnetic field as shown in the sequence of Fig. 9.14, left panel (traces f–i).

Parallel electrical measurements (Fig. 9.14 right panel, traces b–e and traces f–i) demonstrate a similar dependence of the AP time evolution on light/darkness. A transition of a cell from darkness to light prolonged the duration of the membrane depolarization for about 2 s after a transitional

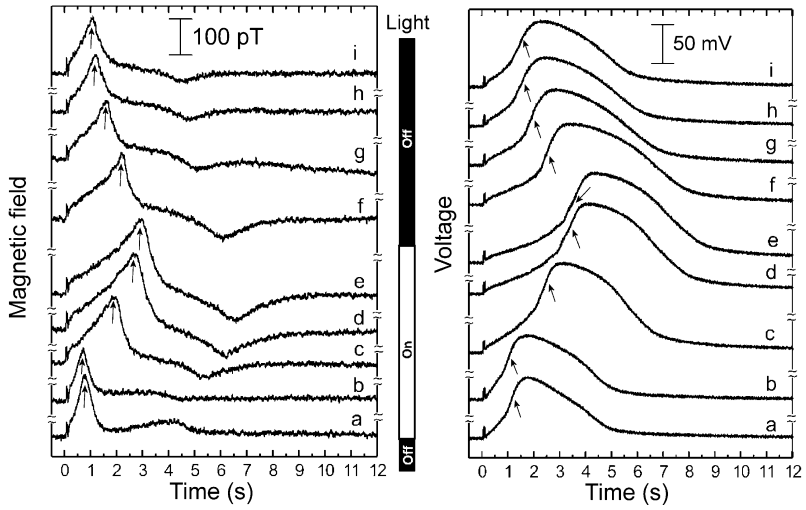

Fig. 9.14. Recordings of the time dependent vertical component of the magnetic field (*left panel*) generated by a propagating AC and simultaneous AP recordings (*right panel*) measured as a function of illumination starting after one hour dark accommodation. Trace *a*, light off, trace *b*, 10 min light on, trace *c*. 20 min light on, trace *d*, 30 min light on, trace *e*, 40 min light on (here we waited for an additional 20 min to complete 1 h in the light accommodation), trace *f*, 10 min light off, trace *g*, 20 min light off, trace *h*, 30 min light off, trace *i*, 40 min light off. *Small arrows* indicate where the temporal shift was observed

period of about 20–30 min on average. The depolarization time prolongation was accompanied by an increase in the depolarization peak of about 10–15%. This can be attributed to the hyperpolarization of the resting potential under illumination (Mimura and Tazawa 1986).

Several tens of internodal cells were measured. They all demonstrate the same behavior under the mentioned sequences of illumination and dark phase. The reversible effect of light/dark transitions on the kinetics of membrane excitation suggests a coupling between photosynthesis and membrane excitation. To examine this hypothesis, the influence of a common photosynthesis inhibitor, DCMU (3,-(3,4-dichlorophenyl)-1,1-dimethylurea) at a concentration of 10 μM on the kinetics of excitation was measured. In this case, a *Chara corallina* cell was exposed to light for a period of 60 min in the presence of DCMU in the bath solution. The light/dark dependent shift in the magnetic signals disappeared, as expected. Two cells were tested with both showing the same behavior.

9.4.2.2 Modeling

The here described light/dark experiments are suitable to demonstrate that the AP in *Chara corallina* shows a similarity to APs in those animal cells (heart,

brain) in which a "biochemical AP" is known. Also in these cases excitation can not be explained by the straight forward Hodgkin–Huxley (HH) (Hodgkin and Huxley 1952) model. Previous work has shown that $[Ca^{2+}]_c$ is altered under the influence of light/dark transitions (Miller and Sanders 1987). The simple HH type mode, which is solely based on the kinetics of plasma membrane channels and electrical properties of the membranes cannot take the changes in $[Ca^{2+}]_c$ into account. In the work of Baudenbacher and co workers (Baudenbacher et al. 2005), an adaptation of the model by Othmer to *Chara* (Wacke et al. 2003) was applied. This model describes the dynamics of $[Ca^{2+}]_c$ in the context of a second messenger system. Using this approach the AP in *Chara* is successfully described by an electrically stimulated release of Ca^{2+} from internal stores. The resulting changes in membrane conductance are the direct consequence of this dynamic change in $[Ca^{2+}]_c$. In this extended model, the threshold-like dependence of Ca^{2+} mobilization on electrical stimulation can be simulated by combining the following two processes:

i. The voltage dependent synthesis/breakdown of the second messenger inositol 1,4,5-trisphosphate (IP_3).
ii. The concerted action of IP_3 and Ca^{2+} on the gating of the receptor channels, which conduct Ca^{2+} release from internal stores.

The model can simulate several experimental results connected to AP in *Chara*. This leads to the conclusion that the all-or-none type activation of the action potential is only the consequence of the preceding all-or-none type mobilization of Ca^{2+} from internal stores. The dependency of the gating of the receptor channel on $[Ca^{2+}]_c$ suggests that the Ca^{2+} concentration prior to stimulation of the AP has an influence on the following excitation kinetics.

To examine the effect of variable $[Ca^{2+}]_c$ on the kinetics of the electrically stimulated changes in Ca^{2+}, we modified the model as follows: cells move excess Ca^{2+} from the cytoplasm back into internal stores by an endogenous Ca^{2+} pump system (e.g. Reddy 2001). In the model, i.e. in the rate equation for Ca^{2+} concentration change with time, this process is accounted for by a Hill function

$$\overline{g}(C) = \frac{\overline{p_1} C^4}{C^4 + \overline{p_2}^4}. \tag{23}$$

In this equation, $\overline{p_1}$ and $\overline{p_2}$ are the Hill coefficients, C is the cytosolic Ca^{2+} concentration. For more details, see Othmer (1997). To achieve different $[Ca^{2+}]_c$ under resting conditions which are known to occur during light/dark transitions (Miller and Sanders 1987; Plieth et al. 1998), the Hill factor $\overline{p_2}$ in Eq. (23) was varied. This procedure is only an indirect approach, since the chloroplasts from which the Ca^{2+} originates during light/dark transitions (Miller and Sanders 1987) are not considered as extra Ca^{2+} pool in the model for $[Ca^{2+}]_c$ dynamics. Nonetheless, this simple manipulation of the model should be sufficient to provide basic insight into the dependency of Ca^{2+} mobilization on $[Ca^{2+}]_c$.

Figure 9.15 illustrates the results of this simulation. As a consequence of a reduced Ca^{2+} pump activity, the resting $[Ca^{2+}]_c$ increases over the physiological range from about 20 nM to 200 nM. This roughly covers the changes in $[Ca^{2+}]_c$ of 50–250 nM found in response to light/dark transitions in *Chara* (Miller and Sanders 1987; Plieth et al. 1998). The simulation further shows that an elevation of $[Ca^{2+}]_c$ prior to the stimulation results in a progressive shortening of the delay time between stimulation and the rapid phase of $[Ca^{2+}]_c$ rise. The dependence of this delay time on the resting $[Ca^{2+}]_c$ concentration is plotted in the inset of Fig. 9.15.

On the assumption that the change in membrane voltage during the AP is only the consequence of an activation of $[Ca^{2+}]_c$ sensitive Cl^-channels (Thiel et al. 1997; Biskup et al. 1999), the model simulation compares well with the light/dark SQUID microscope experimental data. The assumed progressive decrease in $[Ca^{2+}]_c$ of about 150 nM following the transition from dark to light results in an increasing delay time between the electrical stimulus and the rapid phase of $[Ca^{2+}]_c$ rise, or the activation of the Cl^- channels, respectively.

These observed changes in the kinetics of the *Chara* AP could in principle also be modeled by a classical HH approach by adding a variable delay factor. However, there is no mechanistic motivation for such a delay factor and it is difficult to envisage how a first order voltage dependent process such as the voltage dependent activation of plasma membrane channels could produce such a long and variable delay.

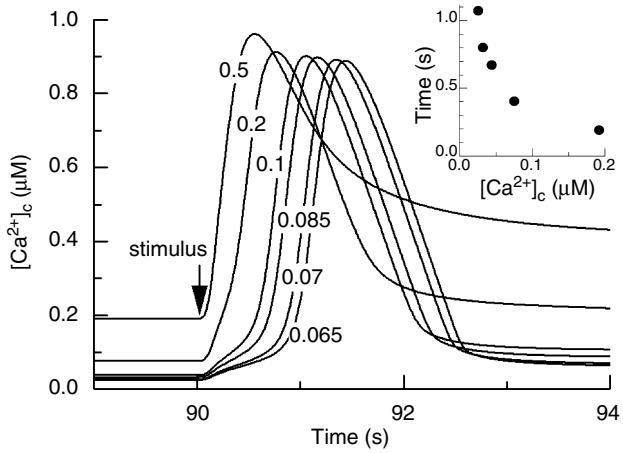

Fig. 9.15. Simulated $[Ca^{2+}]_c$ transients in response to a single electrical stimulation (100 ms/5 µA). Data were calculated with model parameters reported in Wacke et al. (2003). Different curves are obtained by changing the Hill coefficients p_2 in the model term, which describes the buffering of $[Ca^{2+}]_c$. An increase in p_2 over a range of 0.065–0.5 µM results in reduced Ca^{2+} buffering and a consequent increase in the resting $[Ca^{2+}]_c$. In the simulation pulses were started after 90 s in which the system was allowed to equilibrate. Inset: delay time between stimulus and maximal slope of $[Ca^{2+}]_c$ increase as a function of resting $[Ca^{2+}]_c$ before stimulation

Assuming that the activation of the Cl^- channels, which cause the depolarization, is the direct consequence of the change in $[Ca^{2+}]_c$, the measured data nicely match the model prediction, even on a quantitative basis. The model further predicts that a modulation of the resting $[Ca^{2+}]_c$ has no big effect on the kinetics of the bulk changes of $[Ca^{2+}]_c$. Again, this prediction is met by the present data because the features in the temporal evolution of the AC/AP were basically unchanged.

9.4.2.3 Other studies on Chara corallina

Chara corallina is a suitable model system for further investigations using the SQUID magnetometer in different configurations. The authors are aware of (i) research regarding the transnodal conductivity (Belsak 2005) and (ii) preliminary studies of the well known bending phenomenon in *Chara* (Z. Trontelj 2001, private communication).

9.4.3 Magnetic detection of injury induced ionic currents

Magnetic detection of ionic currents was performed also in higher plants. Injury induced quasi-dc ionic currents were detected by the PTB Berlin 49 channel magnetometer (Drung 1995) combined with a suitable modulation on *Vicia faba* plants (Jazbinsek et al. 2000). The temporal and spatial evolution of magnetic field accompanying stimulation by burning and/or cutting of *Vicia faba* plants were measured. Various kinds of local woundings in plants trigger long distance signaling processes. In response to signaling the synthesis of proteins used in defense against insect predators are initiated (Bowles 1990). These proteins which comprise among others protease inhibitors are synthesized not only at the site of wounding but also in distant parts of the plant (Chessin and Zipf 1990; Ryan 1992). This supports the view that at the site of wounding a signal is initiated which is rapidly propagated systemically throughout the plant with the consequence that shortly after the wounding protein synthesis is induced even in parts of the plant distant from the site of wounding (Ryan 1992). Currently, three hypotheses are being discussed for long distant signaling: i) the transmission of a chemical compound in the vessels, ii) propagation of changes in electrical voltage or iii) trauma-evoked hydraulic pressure changes.

Studies using extracellular and intracellular electrodes have revealed that wounding of tissue causes in a variety of plants changes in the electrical membrane voltage (e.g. Roblin 1985; Roblin and Bonnemain 1985; Wildon et al. 1992; Herde et al. 1998). Typically, the electrical response consists of a rapid action potential like depolarization followed by a slower long-lasting depolarization usually termed the variation potential. Wounding induced voltage changes are transmitted from the site of wounding along the plant with a velocity of less than 1 cm/s (Wildon et al. 1992; Roblin and Bonnemein 1995)

and reach the remote tissue before the systemic molecular responses are initiated in this tissue (Stankovic and Davies 1998). From the perspective of magnetic measurements it is important to note that any electric potential difference (voltage) in conducting living tissue is connected with ionic currents. Based on Biot-Savart's law these currents can also be detected magnetically.

To further elucidate the mechanism of electrically based signaling biomagnetic measurements of electrical activity in bean plants have been conducted over the entire plant. This approach takes advantage of the fact that the multichannel SQUID device is able to image electrical activity basically over the whole plant.

For recording the biomagnetic field the currents causing this field should be closed within a large volume. This can be achieved by immersing the whole plant in a suitable ionic solution. This non-invasive and non-touchable method has been used in the past to monitor electrical activity in animal cells, which also respond to injury with electrical activity (Trontelj et al. 1989; Curio et al. 1993). Equivalent to experiments in wounding of animals the measurements with bean plants were aiming to provide information on electrical propagation, injury induced currents and the source of currents in wound stimulated tissue.

One example for a measurement with a cutting injury is shown in Fig. 9.16. In panel (a) of this figure the time evolution of a plant response before introducing a large wound is shown in all 49 channels. Under these conditions, small activity in the area above the plant's leaves can be noticed (dashed lines show the distribution of leaves). Figure 9.16d shows the characteristic isofield map corresponding to the resting situation. There is no indication of symmetry between positive and negative isofield pattern, which is typical for a dipolar isofield pattern. In contrary, there is a dramatic change in the field distribution after cutting the stem and removing the apical part of the plant. A clear symmetric dipolar-like isofield pattern indicates an active localizable current source (Fig. 9.16e). From the time evolution (Fig. 9.16b,c) of the signal $A(B^k)$, defined by Eq. (16), an exponential decay of electrical activity is clearly noticeable. The characteristic decay time was about 10 min.

This biomagnetic measurements on *Vicia faba* plants provide complementary information to electric potential difference measurements on beans (Roblin 1985; Roblin and Bonnemain 1985) and other plant species in responds to local wounding (e.g. Wildon et al. 1992; Herde et al. 1998). This additional information is obtained non-invasively and without touching the plant. In some cases where the isofield maps were obtained in the form close to the dipolar field distribution, an equivalent current dipole (ECD) was used to model the magnetic field distribution over the *Vicia faba* plant. Though it is difficult to find an electrophysiologic explanation for this type of current source in most cases, it seems to be a reasonable description of a current source in the case of a big wound (Fig. 9.16e). In this case, a strong localizable flow of ions takes place at the wound. The estimated ECD strength p and

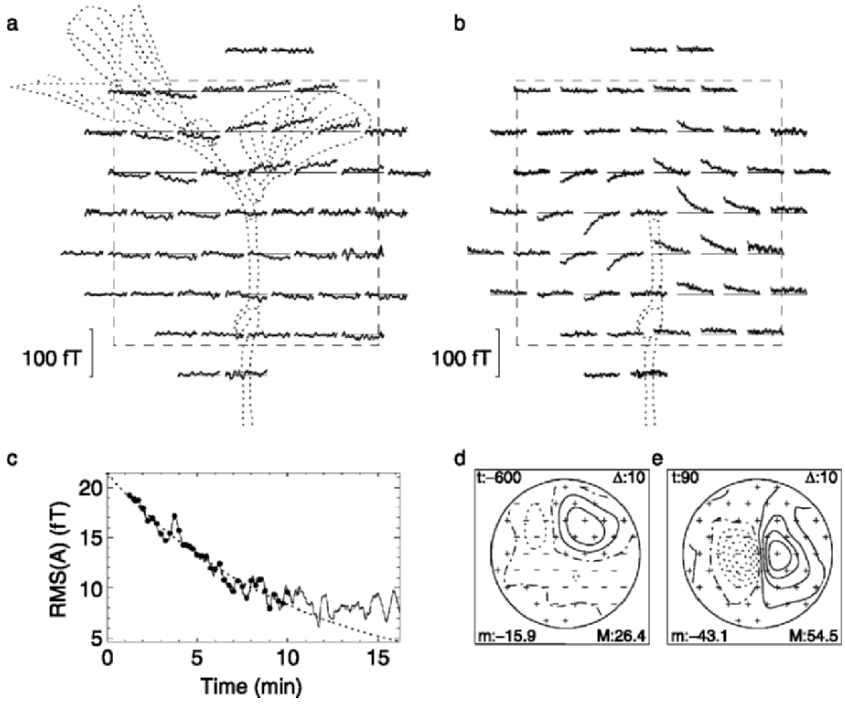

Fig. 9.16. Time evolution of magnetic field in all channels: **a** 25-10 min before cutting the plant and **b** 1–16 min after cutting. Sketch of plant is shown with *dotted lines* and inner side of the chamber is indicated by *dashed line*. **c** *Solid line* represents time evolution of injury related RMS magnetic field from **b**, bullets shows RMS values of magnetic field each 15 s in the first 10 min after the injury. These values were fitted with exponential decay function shown by dotted line. **d** and **e** isofield maps 10 min before and 1.5 min after the injury, respectively. Here t denotes time from the injury in *s*, m and M are minimal and maximal field values in *fT*, and Δ step between two isofield lines in *fT*. Solid, dash-dot-dash and dot line styles represent positive, zero and negative isofield lines, respectively. Positions of magnetic sensors are shown by + and – in accordance with the measured field sign

current J associated with the ionic transport obtained 1.5 min after the cutting injury were 6.6 nAm and 0.14 μA, respectively. The maximal currents obtained in plants with burning stimulation were between 0.1 and 0.24 μA. These values were estimated from the ECD strength p and the source length $2a$ ($J=p/2a$). From this current one can estimate the average order of magnitude for the current density of 0.01 μA/mm^2, where it is assumed that the bean stem cross-section is approximately 20 mm^2. The localization of maximal electrical activity—the position of equivalent current source—overlaps with the stem location with accuracy of better than 1 cm.

All investigated plants responded to stimulation by burning or cutting and the phenomenon was magnetically detected. Magnetic measurements could

not confirm a long distance spreading of electric activity. Correspondingly, it is not yet possible to favor one of the three possible hypotheses on long distance signaling in wounded plants.

Acknowledgement We thank to the colleagues from the Physikalisch-Technische Bundesanstalt, Institut Berlin, where the first biomagnetic measurements on the internodal cell of Chara corallina were performed, as well as to the colleagues from the Living state group of the Department of Physics and Astronomy of the Vanderbilt University, Nashville, TN, where the first SQUID microscopy measurements on Chara corallina cells were done. We also thank to the Biophysical Journal for the permission of reprinting Figs. 9.5, 9.6, 9.7, 9.8, 9.12, 9.13 and 9.15, as well as to the European Biophysics Journal for the permission of reprinting Fig. 9.16.

References

Baluska F, Volkmann D, Menzel D (2005) Plant synapses: actin-based domains for cell-to-cell communication. Trends Plant Sci 10:106–111

Barr RC, Ramsey M, Spach MS (1977) Relating epicardial to body-surface potential distributions by means of transfer-coefficients based on geometry measurements. IEEE T Biomed Eng 24:1–11

Bardeen J, Cooper LN, Schrieffer JR (1957) Theory of superconductivity. Phys Rev 5:1175–1204

Baudenbacher F, Peters NT, Wikswo JP (2002) High resolution low-temperature superconductivity superconducting quantum interference device microscope for imaging magnetic fields of samples at room temperatures. Rev Sci Instrum 73:1247–1254

Baudenbacher F, Fong LE, Thiel G, Wacke M, Jazbinsek V, Holzer JR, Stampfl A, Trontelj Z (2005) Intracellular axial current in *Chara corallina* reflects the altered kinetics of ions in cytoplasm under the influence of light. Biophys J 88:690–697

Bauer CS, Plieth C, Hansen UP, Sattelmacher B, Simonis W, Schonknecht G (1997) Repetitive Ca^{2+} spikes in a unicellular green alga. FEBS Lett 405:390–393

Bentrup FW (1979) Reception and transduction of electrical and mechanical stimuli. In: Haupt W, Feinleib ME (eds) Physiology of movement. Encyclopedia of plant physiology, new series. Springer, Berlin Heidelberg New York

Bednorz JG, Mueller KA (1986) Possible high Tc superconductivity in the barium-lanthanum-copper-oxygen system. Z Phys B 64:189–193

Beilby MJ (1990) Current-voltage curves for plant membrane studies: a critical analysis of the method. J Exp Bot 41:165–182

Belsak M (2005) Diploma thesis, Faculty of Mathematics and Physics, University of Ljubljana

Berestovsky GN, Kataev AA (2002) Voltage-gated calcium and Ca^{2+}-activated chloride channels and Ca^{2+} transients: voltage-clamp studies of perfused and intact cells of Chara. Eur Biophys J (published online)

Berestovsky GN, Kataev AA (2005) Voltage-gated calcium and Ca^{2+}-activated chloride channels and Ca^{2+} transients: voltage-clamp studies of perfused and intact cells of Chara. Eur Bio J 34:973–986

Biskup B, Gradmann D, Thiel G (1999) Calcium release from $InsP_3$-sensitive internal stores initiates action potential in chara. FEBS Lett 453:72–76

Bowles DJ (1990) Defence-related proteins in higher plants. Annu Rev Biochem 59:873–907

Brebbia CA, Telles JCF, Wrobel LC (1984) Boundary element techniques: theory and applications in engineering. Springer, Berlin Heidelberg New York

Burnett DS (1987) Finite element analysis. Addison-Wesley, Reading, MA

Chavis P, Fagni L, Lansman JB, Bockaert J (1996) Functional coupling between ryanodine receptors and L-type calcium channels in neurons. Nature 382:719–722

Chessin M, Zipf AE (1990) Alarm systems in higher plants. Bot Rev 56:193–235

Clark J, Plonsey R (1966) A mathematical evaluation of the core conductor model. Biophys J 6:95–112

Clint GM, MacRobbie EAC (1987) Sodium efflux from perfused giant algal cells. Planta 171:247–253

Curio G, Erné SN, Burghoff M, Wolff H-D, Pilz A (1993) Non-invasive neuromagnetic monitoring of nerve and muscle injury currents. Electroenceph Clin Neurophys 89:154–160

Deaver BS, Fairbank WM (1961) Experimental evidence for quantized flux in superconducting cylinders. Phys Rev Lett 7:43–46

Drung D (1995) The PTB 83-SQUID system for biomagnetic applications in a clinic. IEEE T Appl Supercon 5:2112–2117

Erné SN, Hahlbohm D, Scheer H, Trontelj Z (1981) Berlin magnetically shielded room (BMSR). In: Erné SN, Hahlbohm D, Lübbig H (eds) Biomagnetism, Proceedings of the Third International Workshop on Biomagnetism, Berlin, May 1980. Walter de Gruyter, Berlin, pp 79–89

Findlay GP, Hoppe AB (1976) Electrical properties of plants. In: Luttge U, Pitman MG (eds) Transport in plants II. Springer, Berlin Heidelberg New York, pp 79–92

Gradmann D (1976) "Metabolic" action potentials in *Acetabularia*. J Membr Biol 29:23–45

Gradmann D, Blatt MR, Thiel G (1993) Electrocoupling of ion transporters in plants. J Membr Biol 136:327–332

Hämäläinen MS, Ilmoniemi RJ (1994) Interpreting magnetic fields of the brain: minimum-norm estimates. Med Biol Eng Comput 32:35–42

Hansen PC (1992) Numerical tools for analysis and solution of Fredholm integral-equations of the 1st kind. Inverse Problems 8:849–872

Herde O, Pena-Cortes H, Willmitzer L, Fisahn J (1998) Remote stimulation by heat induces characteristic membrane-potential responses in the vein of wild-type and abscisic acid-deficient tomato plants. Planta 206:146–153

Hodgkin AL, Huxley AF (1952) A quantitative description of membrane current and its application to conductance and excitation in nerve. J Physiol Lond 117:500–544

Homann U, Thiel G (1994) Cl^- and K^+ channel currents during the action potential in chara; simultaneous recording of membrane voltage and patch currents. J Membrane Biol 141:297–309

Hope AB, Findlay GP (1964) The action potential in chara. Plant Cell Physiol 5:377–379

Hope AB, Walker NA (1975) Physiology of giant algal cells. Cambridge University Press, London

Jaklevic RC, Lambe J, Silver AH, Mercereau JE (1964) Quantum interference effects in Josephson tunneling. Phys Rev Lett 12:159–160

Jazbinsek V, Thiel G, Wübbeler G, Müller W, Trontelj Z (2000) Magnetic detection of injury-induced ionic currents in bean plants. Eur Biophys J 29:515–522

Josephson BD (1962) Possible new effects in superconductive tunnelling. Phys Lett 1:251–253

Kikuyama M, Tazawa M (1983) Transient increase of intracellular Ca^{2+} during excitation of tonoplast-free chara cells. Protoplasma 117:62–67

Koch H, Cantor R, Erné SN, Matthies KP, Peters M, Ryhänen T, Scheer HJ, Hahlbohm HD (1991) A 37 channel dc-SQUID magnetometer system. IEEE Trans Magn 27:2793–2796

Kotani M, Uchikawa Y, Kawakatsu M, Tsukada K, Kandori A, Sasabuti H, Suzuki H, Kondo S, Matsuda N, Shinada K, Yamada Y (1997) A whole-head SQUID system for detecting vector components. Appl Supercon 5:399–403

Miller AJ, Sanders D (1987) Depletion of cytosolic free calcium induced by photosynthesis. Nature 326:397–400

Mimura T, Tazawa M (1986) Light-induced membrane hyperpolarization and adenin nucleotide levels in perfused characean cells. Plant Cell Physiol 27:319–330

Moriyasu Y, Shimmen T, Tazawa M (1984) Electric characteristics of the vacuolar membrane of Chara in relation to pHv regulation. Cell Struct Funct 9:235–246

Nelson MT, Cheng H, Rubart M, Santana LF, Bonev AD, Knot HJ, Lederer WJ (1995) Relaxation of arterial smooth muscle by calcium sparks. Science 270:633–637

Okihara K, Ohkawa T, Tsutsui I, Kasai M (1991) A calcium dependent and voltage-dependent chloride-sensitive anion channel in the chara plasmalemma. A patch clamp study. Plant Cell Physiol 32:593–602

Onnes HK (1911) The superconductivity of mercury. Comm Phys Lab 12:120
Othmer HG (1997) Signal transduction and second messenger systems. In: Othmer HG, Adler FR, Lewis MA, Dallon J (eds) Case studies in mathematical modeling—ecology, physiology and cell biology. Prentice Hall, Upper Saddle River, New Jersey, pp 99–126
Pena-Cortes H, Fisahn J, Willmitzer L. (1995) Signals involved in wound-induced proteinase inhibitor II gene expression in tomato and potato plants. Proc Natl Acad Sci USA. 92:4106–4113
Parker RL (1977) Understanding inverse theory. Annu Rev Earth Planet Sci 5:35–64
Plieth C, Sattelmacher B, Hansen UP (1998) Light-induced cytosolic calcium transients in green plant cells. I. Methodological aspects of chlorotetracycline usage in algae and higher-plant cells. Planta 207:42–51
Plonsey R (1969) Bioelectric phenomena. McGraw-Hill, New York
Ramsey M, Barr RC, Spach MS (1977) Comparison of measured torso potentials with those simulated from epicardial potentials for ventricular depolarization and repolarization in intact dog. Circ Res 41:660–667
Reddy ASN (2001) Calcium: silver bullet in signalling. Plant Sci 160:381–404
Rhodes JD, Thain JF, Wildon DC (1996) The pathway for systemic electrical signal conduction in the wounded tomato plant. Planta 200:50–57
Roblin G (1985) Analysis of the variation potential induced by wounding in plants. Plant Cell Physiol 26:455–461
Roblin G, Bonnemain J-L (1985) Propagation in *Vicia faba* stem of a potential variation induced by wounding. Plant Cell Physiol 26:1273–1283
Ryan CA (1992) The search for the proteinase-inhibitor inducing factor PIIF. Plant Mol Biol 19:123–133
Sarvas J (1987) Basic mathematical and electromagnetic concepts of the biomagnetic inverse problem. Phys Med Biol 32:11–22
Shimmen T, Mimura T, Kikuyama M, Tazawa M (1994) Characean cells as a tool for studying electrophysiological characteristics of plant cells. Cell Struct Funct 19:263–278
Slibar M, Trontelj Z, Jazbinsek V, Thiel G, Mueller W (2000) Magnetic field and electric potential of excited plant cell *Chara corallina*: calculation and comparison with experiment. In: Aine CJ, Okada Y, Stroink G, Swithenby SJ, Wood CC (eds) Biomag 96: proceedings of the 10th international conference on biomagnetism. Springer, Berlin Heidelberg New York, pp 679–682
Stankovic B, Davies E (1998) The wound response in tomato involves rapid growth and electrical responses, systemically up-regulated transcription of proteinase inhibitors and calmodulin and down regulated translation. Plant Cell Physiol 39:268–274
Stratton JA (1941) Electromagnetic theory. McGraw-Hill, New York
Tazawa M, Kikuyama M (2003) Is Ca^{2+} release from internal stores involved in membrane excitation in characean cells? Plant Cell Physiol 44:518–526
Tester M (1990) Plant ion channels: whole-cell and single channel studies. New Phytol 114:305–340
Thiel G, Homann U, Plieth C (1997) Ion channel activity during the action potential in chara: new insights with new techniques. J Exp Bot 48:609–622
Tinkham M (1996) Introduction to superconductivity, second edition. McGraw-Hill, Inc., New york.
Trahms L, Erné SN, Trontelj Z, Curio G, Aust P (1989) Biomagnetic functional localization of a peripheral-nerve in man. Biophys J 55:1145–1153
Trontelj Z, Pirnat J, Luznik J, Jazbinsek V, Valencic V, Krizaj D, Vodovnik L, Jercinovic A (1989) Measurement of magnetic field near an acute surgical Injury on the rabbit's thigh. In: Williamson SJ, Hoke M, Stroink G, Kotani M (eds) Advances in biomagnetism. Plenum Press, New York, pp 517–520
Trontelj Z, Zorec R, Jazbinsek V, Erné SN (1994) Magnetic detection of a single action potential in *Chara corallina* internodal cells. Biophys J 66:1694–1696
Umrath K (1929) Über Erregungsleitung bei höheren Pflanzen. Planta 7:174–207

Wacke M, Thiel G (2001) Electrically triggered all-or-none Ca^{2+} liberation during action potential in the giant alga chara. J Gen Physiol 118:11–21

Wacke M, Thiel G, Hütt MT (2003) Ca^{2+} dynamics during membrane excitation of green alga chara: model simulations and experimental data. J Membr Biol 191:179–192

Wikswo JP, Barach JP, Freeman JA (1980) Magnetic-field of a nerve impulse—1st measurements. Science 208:53–55

Wildon DC, Thain JF, Minchin PEH, Gubb IR, Reilly AJ, Skipper YD, Doherty HM, O'Donnell PJ, Bowles DJ (1992) Electrical signalling and systemic proteinase inhibitor induction in the wounded plant. Nature 360:62–65

Williamson RE, Ashley CC (1982) Free Ca^{2+} and cytoplasmic streaming in the alga chara. Nature 296:647–651

Williams SE, Pickard B (1972) Receptor potentials and action potentials in Drosera tentacles. Planta 103:193–221

Woosley JK, Roth BJ, Wikswo JP (1985) The magnetic field of a single axon: a volume conductor model. Math Biosci 76:1–36

Wübbeler G, Mackert J, Armbrust F, Burghoff M, Mackert B, Wolff K-D, Ramsbacher J, Curio G, Trahms L (1998) SQUID measurements of human nerve and muscle near-DC injury-currents using a mechanical modulation of the source position. Appl Supercond 6:559–565

Zimmerman JE, Thiene P, Harding JT (1970) Design and operation of stable RF-biased superconducting point-contact quantum devices, and a note on properties of perfectly clean metal contacts. J Appl Phys 41:1572–1580